



# A Heterogeneous Quasi-solid-State Hybrid Electrolyte Constructed from Electrospun Nanofibers Enables Robust Electrode/Electrolyte Interfaces for Stable Lithium Metal Batteries

Manxi Wang<sup>1</sup> · Shiwen Lv<sup>1</sup> · Manxian Li<sup>1</sup> · Xuan Li<sup>1</sup> · Chuanping Li<sup>1</sup> · Zulin Li<sup>1</sup> · Xiaochuan Chen<sup>1</sup> · Junxiong Wu<sup>1</sup> · Xiaoyan Li<sup>1</sup> · Yuming Chen<sup>1,2</sup> · Qinghua Chen<sup>1</sup>

Received: 30 September 2023 / Accepted: 27 December 2023 / Published online: 27 February 2024  
© Donghua University, Shanghai, China 2024

## Abstract

Quasi-solid-state electrolytes that possess high ionic conductivity, excellent interface stability, and low interfacial resistance, are required for practical solid-state batteries. Herein, a heterogeneous quasi-solid-state hybrid electrolyte (QSHE) with a robust lithium-ion transport layer composed of  $\text{Li}_{1+x}\text{Al}_x\text{Ti}_{2-x}(\text{PO}_4)_3$  (LATP) nanoparticles (NPs) at the anode/electrolyte interface was fabricated using electrospun nanofibers as a skeleton via a facile in situ polymerization approach. The QSHE exhibits a high ionic conductivity ( $0.98 \text{ mS cm}^{-1}$ ), a wide electrochemical window ( $4.76 \text{ V vs. Li/Li}^+$ ), and favorable compatibility with lithium metal (maintaining stability over 2000 h in a symmetrical cell) at room temperature. When coupled with a  $\text{LiLiFePO}_4$  battery, the QSHE enables the battery to retain 95.4% of its capacity after 300 cycles at 2 C. Moreover, the atomic force microscopy verifies the high Young's modulus of the LATP-dominated bottom layer, while numerical simulation validates the effective distribution of lithium ions at the interface facilitated by LATP NPs, hence contributing to dendrite-free lithium plating/stripping morphology. This straightforward strategy could pave the way for the development of high-performance and interfacially stable lithium metal batteries.

**Keywords** In situ polymerization · Quasi-solid-state electrolytes · Interface compatibility · Lithium dendrites

---

Manxi Wang and Shiwen Lv contributed equally to the work.

- ✉ Xiaochuan Chen  
chenxch29@126.com
- ✉ Junxiong Wu  
jwuba@fjnu.edu.cn
- ✉ Xiaoyan Li  
xiaoyanli1985@126.com
- ✉ Yuming Chen  
yuminc126@126.com

<sup>1</sup> Engineering Research Center of Polymer Green Recycling of Ministry of Education, Fujian Key Laboratory of Pollution Control and Resource Reuse, College of Environmental and Resource Sciences and College of Carbon Neutral Modern Industry, Fujian Normal University, Fuzhou 350000, China

<sup>2</sup> State Key Laboratory of Structural Chemistry, Fujian Institute of Research on the Structure of Matter, Chinese Academy of Sciences, Fuzhou 350000, China

## Introduction

The surging demand for electric vehicles and grid energy storage has accelerated the development of high-energy-density batteries [1–4]. Among various rechargeable batteries, lithium (Li) metal batteries are deemed as a promising candidate because the use of Li metal anode offers significant advantages, including a remarkable theoretical capacity of  $3860 \text{ mAh g}^{-1}$  and an ultralow redox potential of  $-3.04 \text{ V vs. standard hydrogen electrode}$  [5–8]. However, conventional carbonate-based liquid electrolytes (LE) are detrimental to Li metal due to unwanted side reactions, resulting in low plating/stripping Coulombic efficiency (CE) and hazardous dendrite growth [9–11]. In addition to the above challenges, the leakage of LEs also poses a risk to the safe operation of batteries. Hence, the development of solid-state electrolytes has attracted tremendous research attention [12, 13].

All-solid-state electrolytes (ASSEs) are currently based on polymers and ceramics [14–16]. Polymer-based solid-state electrolytes (SSEs) require high operating temperatures

to elevate their ionic conductivities, but their low mechanical strength cannot prevent lithium dendrite growth [17, 18]. Ceramic-based SSEs, while demonstrating high ionic conductivities ranging from  $10^{-4}$  to  $10^{-3}$  S  $\text{cm}^{-1}$  at room temperature and ultra-high mechanical strength, suffer from high interface impedances between the inorganic ASSE and the electrode due to the solid–solid contact, leading to large cell polarization [19–21]. The introduction of a small amount of LE to improve the electrode/electrolyte interfaces has been suggested but compromises battery safety performance [22]. Therefore, novel SSEs that can operate at room temperature, suppress lithium dendrite growth, and achieve good interface contact with electrodes are highly desired [23].

Quasi-solid-state polymer electrolytes (QSPEs) produced by in situ polymerized have attracted significant interest because of their seamless contact with electrodes, resulting in small interfacial resistances [24, 25]. By incorporating various salts and novel additives to improve the ionic conductivity [26–28], in situ polymerized QSPEs have featured unique functionalities, including single-ion conductor [29], thermal failure/flammability retardancy [30], wide working temperature range [31, 32]. Nevertheless, the current polymerization methods involving heating and ultraviolet radiation are relatively intricate, impeding their practical utilization [33]. Simple polymerization methods for QSPEs that can accelerate their commercialization through a realistic roll-to-roll production process need to be explored. The commonly used solvent, 1, 3-dioxolane (DOL), in Li metal batteries shows great potential for commercial applications as it can be initiated by commonly used lithium salts [34–36] at room temperature, and the resulting polymerized DOL (PDOL) has good compatibility against Li metal [37]. Ma et al. [38] mixed DOL with a carbonate-based solvent to expand the redox window of the electrolyte, and the  $\text{LiPF}_6$ -initiated solid/liquid hybrid electrolyte exhibited excellent compatibility with a nickel-rich layered oxide cathode ( $\text{LiNi}_{0.8}\text{Co}_{0.1}\text{Mn}_{0.1}\text{O}_2$ ). Liu and co-workers [34] introduced trioxymethylene to partially inhibit the polymerization of DOL, aiming to further improve the ionic conductivity by leveraging unpolymerized DOL as a plasticizer. In addition, Huang et al. [39] introduced 1,1,2,2-tetrafluoroethyl 2,2,3,3-tetrafluoropropyl ether (TTE) into PDOL to regulate the solvation structure, leading to a QSPE with enhanced cycle stability under high voltage. However, the limited strength of PDOL is insufficient to inhibit the growth of lithium dendrites. It should be noticed that the current studies primarily focus on the preparation of homogeneous QSPEs, while the development of heterogeneous quasi-solid-state hybrid electrolytes (QSHEs) featuring a robust inorganic rich layer at the Li metal side is expected to effectively alleviate lithium dendrite growth.

In this work, a heterogeneous QSHE with an inorganic component-rich bottom layer was prepared through

in situ polymerization using a conventional  $\text{LiPF}_6$  salt.  $\text{Li}_{1+x}\text{Al}_x\text{Ti}_{2-x}(\text{PO}_4)_3$  (LATP) nanoparticles (NPs) were selected as the inorganic filler to enhance the overall ionic conductivity and Young's modulus of the bottom region due to its high ionic conductivity and mechanical strength. Concurrently, an electrospun polyvinylidene fluoride-hexafluoropropylene (PVDF-HFP) nanofiber membrane, with the strong electro-withdrawing effect provided by C–F groups, was employed to encapsulate the DOL precursor solution, forming a 3D  $\text{Li}^+$  transport network [40–42]. During polymerization, the added LATP NPs will simultaneously deposit on the side near the Li metal due to gravity, thereby promoting the transport of  $\text{Li}^+$  through the interface, as depicted in Fig. 1. Although LATP was reported to react with Li [43], sufficient wetting and filling of the precursor polymer solution at the electrode interface mitigate the side reactions between Li and LATP [44]. Importantly, the QSHE possessed an average Young's modulus of  $\sim 3.2$  GPa at the ceramic-rich region facing the Li anode, surpassing that of homogeneous QSPE. The ceramic-rich (bottom) region with high Young's modulus in the QSHE ensures efficient resistance against the Li dendrites and the soft polymer-rich (top) layer minimizes the interfacial impedances. Furthermore, COMSOL simulation results demonstrated that LATP NPs also act as a  $\text{Li}^+$  ion redistributor to alleviate the concentration gradient in the cells, facilitating a more uniform deposition of Li. As a result, the Li|Li symmetric cells with the QSHE demonstrated stable polarization curves for more than 2000 h, and the assembled Li|LiFePO<sub>4</sub> (LFP) cells displayed excellent cyclic performance and rate capability.

## Experimental Section

### Materials

LFP (battery grade), conductive carbon black, polyvinylidene difluoride (PVDF, Arkema900), *N*-methyl-2-pyrrolidone (NMP, Aladdin; AR), PVDF-HFP (Sigma;  $M_w = 455,000$ ), *N,N*-dimethylformamide (DMF, SCR; AR), lithium di(trifluoromethyl sulfonyl) imide (LiTFSI, DoDoChem; 99.5%), lithium hexafluorophosphate ( $\text{LiPF}_6$ , DoDoChem; 99.9%),  $\text{Li}_{1.3}\text{Al}_{0.3}\text{Ti}_{1.7}(\text{PO}_4)_3$  (Canrd; 300 nm), DOL (DoDoChem; 99%), methyl propionate (MP, Aladdin; 99%), fluoroethylene carbonate (FEC, DoDoChem; 99.9%), and commercial liquid electrolyte (1 M  $\text{LiPF}_6$  in dimethyl carbonate: ethylene carbonate = 7:3 vol.%) were used as received. All the solid powders or particles used in this study were dried at 80 °C over 12 h, and the DOL, MP, and FEC were dehydrated by molecular sieve (DoDoChem; 4A) in a glove box (Mikrouna) over 24 h before use.

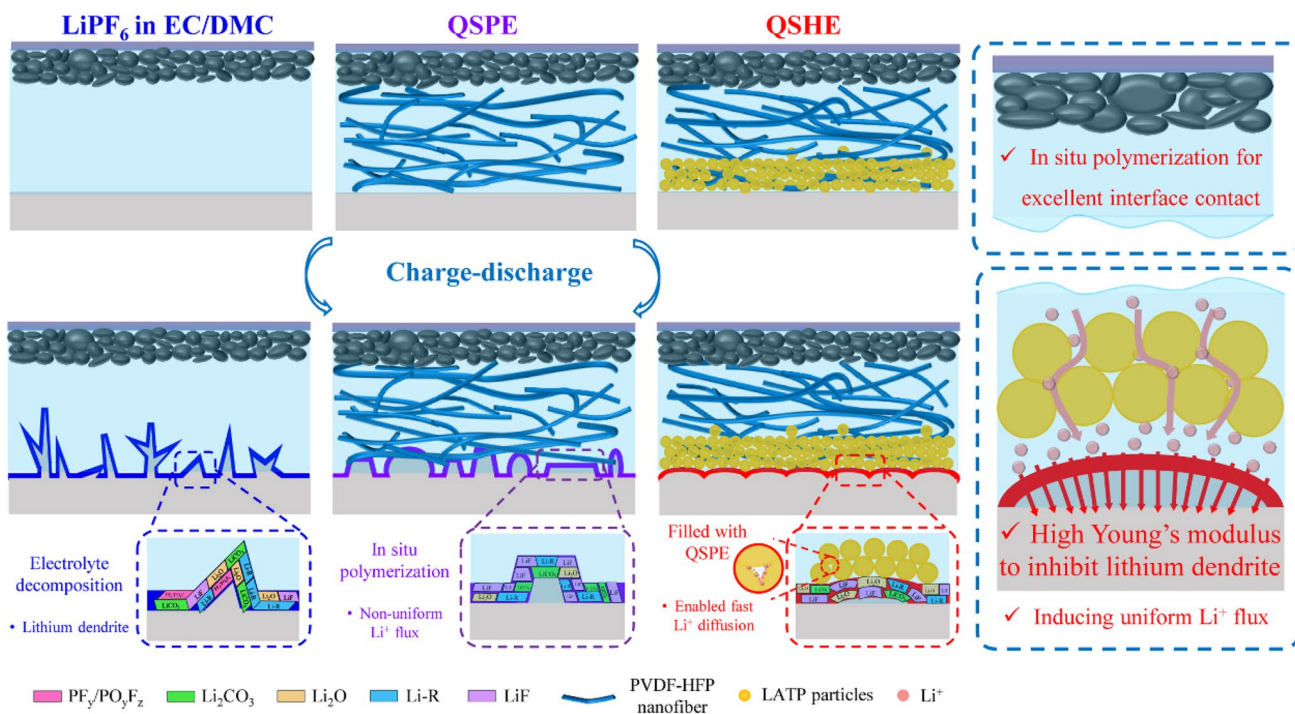


Fig. 1 Diagram of different lithium deposition behaviors in LE, QSPE, and QSHE

### Preparation of LFP Cathode

LFP, carbon black, and PVDF at a mass ratio of 8:1:1 were dissolved in NMP to prepare a homogeneous slurry, which was then coated on the aluminum foil through a simple doctor blade. The LFP electrode was then dried in a vacuum oven at 80 °C for 12 h to ensure complete volatilization of NMP. The mass loading of the as-prepared LFP electrode was ~3.5 mg cm<sup>-2</sup>.

### Preparation of Electrospun PVDF-HFP Matrix

The precursor solution for electrospinning was prepared by dissolving 2.1 g PVDF-HFP in 10 mL DMF overnight. A 10 mL syringe fitted with an 18G needle (inner diameter: 0.92 mm, external diameter: 1.28 mm) was used to load the precursor solution. During electrospinning, a high voltage of 20 kV was applied with a feeding rate of 1.0 mL h<sup>-1</sup>. Notice that the humidity during electrospinning was controlled at ~40%. The obtained PVDF-HFP membrane was dried at 80 °C overnight for further use.

### Preparation of In Situ Polymerized QSPE/QSHE and Cell Assembly

**QSPE:** The preparation of electrolytes was carried out inside a glove box filled with pure argon gas (O<sub>2</sub> < 0.1 ppm, H<sub>2</sub>O < 0.1 ppm). Firstly, 1.0 M LiTFSI was dissolved in a

mixed solution of DOL and FEC (5:1, vol.%), and 0.5 M LiPF<sub>6</sub> was dissolved in MP, respectively. After that, the above two solutions were mixed with a volume ratio of 3:2 and stirred for 10 min to form a homogeneous precursor. During battery assembly, 60 μL of the precursor solution was dropped into the trimmed PVDF-HFP membrane. Finally, the assembled cells were laid up for 24 h to allow the spontaneous polymerization of precursor solution, thus obtaining in situ polymerized QSPE inside the batteries.

**QSHE:** in contrast to QSPE, 20 wt.% LATP particles were added to the vial with the mixed solution. The polymerization of the solution containing LATP particles in the PVDF-HFP membrane was denoted as QSHE.

### Material Characterizations

The porosity of the electrospun PVDF-HFP was measured through the n-butanol absorption method. The sample with a diameter of 16 mm was immersed in n-butanol for 2 h and then blotted the excess liquid on the surface with filter paper. The porosity was calculated based on Eq. (1) listed below [45]:

$$\text{Porosity}(\%) = \frac{W_{\text{wet}} - W_{\text{dry}}}{\rho V_{\text{dry}}} \tag{1}$$

where  $W_{\text{dry}}$  and  $W_{\text{wet}}$  are the mass of membranes before and after soaking,  $\rho$  and  $V_{\text{dry}}$  represent the density of n-butanol and the volume of membranes, respectively.

The electrolyte uptake was measured by immersing the PVDF-HFP membranes into the liquid electrolyte, i.e., 1 M LiPF<sub>6</sub> in ethylene carbonate: dimethyl carbonate = 3:7, vol.%, for 2 h, which was calculated using the following Eq. (2) [45]:

$$\text{Electrolyte uptake (\%)} = \frac{W_2 - W_1}{W_1} \quad (2)$$

where  $W_1$  and  $W_2$  are the mass of membranes before and after immersion in the electrolyte.

The morphology of pure nanofiber membrane, QSPE, QSHE, and cycled lithium was observed by scanning electron microscope (SEM; Regulus 8100). The polymerized electrolyte was placed in the glove box for 48 h to remove the residual liquid. Energy dispersive spectroscopy (EDS) was used to characterize the element distribution of the samples. The structures of QSPE and QSHE were identified by X-ray diffractometer (XRD; Bruker, D8 ADVANCE) at a rate of 10 °C min<sup>-1</sup> in the scanning range of 5°–60°. The Young's modulus of the QSHE and QSPE electrolytes were measured through atomic force microscopy (AFM; Bruker, NanoWizard 4). Nuclear magnetic resonance spectroscopy (NMR; JEOL, JNM-ECZ600R/S1) was conducted to collect the <sup>1</sup>H-NMR and <sup>13</sup>C-NMR spectra with dimethyl sulfoxide (DMSO-*d*<sub>6</sub>) serving as the deuterated solvent. Fourier transform infrared spectroscopy (FTIR; NICOLET IS10) was conducted to examine the chemical structure of DOL before and after polymerization, and the polymerization degree was further determined using gel permeation chromatography (GPC; 1260 infinity II). The thermal stability of QSPE and QSHE was studied using a thermogravimetric analyzer (TGA; TGA, Q50) with a heating rate of 10 °C min<sup>-1</sup> from 30 to 600 °C in a nitrogen atmosphere. A differential scanning calorimeter (DSC; TA, DSC25) was also applied under the nitrogen atmosphere to test the glass transition temperature ( $T_g$ ) from -80 to 40 °C and the heating and cooling rates were 10 °C min<sup>-1</sup>. The solid electrolyte interphase (SEI) composition on the cycled Li metal anodes was characterized using X-ray photoelectron spectroscopy (XPS; Thermo Fisher, ESCALAB Xi+).

## Electrochemical Characterizations

CR2032-type coin cells were assembled in a glove box filled with pure argon gas (O<sub>2</sub> < 0.1 ppm, H<sub>2</sub>O < 0.1 ppm). Stainless steel (SS)|QSPE/QSHE|SS cells were assembled to measure the ionic conductivity ( $\sigma$ ) and activation energy of QSPE/QSHE by electrochemical impedance spectroscopy (EIS), the frequency range was set at 0.1 Hz–100 kHz from -30 to 30 °C using an electrochemical workstation (CHI760E). The ionic conductivity was calculated by:

$$\sigma = \frac{L}{RS} \quad (3)$$

where  $L$  and  $S$  are the thickness and contact area of electrolytes and  $R$  is the bulk resistance. The temperature-dependent ionic conductivity was fitted with the Vogel–Tamman–Fulcher equation [46] to calculate the activation energy ( $E_a$ ) of the electrolyte:

$$\sigma = \sigma_0 \cdot T^{-\frac{1}{2}} \exp\left(-\frac{E_a}{k_B(T - T_0)}\right) \quad (4)$$

where  $\sigma_0$  and  $k_B$ , respectively, represent the pre-exponential factor and Boltzmann constant.  $T_0$  refers to the reference temperature which typically falls 10–50 K below  $T_g$ . Here, a  $T_0$  value 50 K below  $T_g$  was used for calculation. The Li<sup>+</sup> transference number ( $t_{Li^+}$ ) was determined by combined methods of direct current polarization and EIS using Li|Li symmetric cells. The applied polarization voltage ( $\Delta V$ ) and alternating current impedance frequency were 10 mV and 1 MHz–1 Hz, respectively. The values of  $t_{Li^+}$  could be calculated by the following equation [46]:

$$t_{Li^+} = \frac{I_S(\Delta V - I_0 R_0)}{I_0(\Delta V - I_S R_S)} \quad (5)$$

where  $I_0$  and  $I_S$  are the initial and steady-state current,  $R_0$  and  $R_S$  are the initial and steady-state interfacial resistances. The electrochemical stable window (ESW) was tested by linear sweep voltammetry (LSV) with Li|QSPE/QSHE|SS cells with a scan rate of 1 mV s<sup>-1</sup> between 2.0 and 6.0 V vs. Li/Li<sup>+</sup>. Cyclic voltammetry (CV) of Li|QSPE/QSHE|LFP was measured at different scan rates ( $v$ ). Based on the Randles–Sevcik equation [33], the Li<sup>+</sup> diffusion coefficient ( $D_{Li}$ ) of QSHE and QSPE was calculated according to Eq. (5):

$$i_p = 269,000 n^{\frac{3}{2}} A C_{Li} D_{Li}^{\frac{1}{2}} v^{\frac{1}{2}} \quad (6)$$

where  $i_p$  stands for the peak current,  $n$  is the number of electrons involved in the redox reaction and  $A$  is the active area of the electrode.  $C_{Li}$  is the concentration of Li<sup>+</sup> transferred in the charge–discharge process.

To evaluate the performance of QSHE and QSPE, Li|Li, Li|Cu, and Li|LFP cells were assembled and tested using the LANHE battery testing system (CT3001A). When the Li|QSHE|Cu cells were assembled, the LTP-rich side of QSHE was designed to face the copper foil for a fair comparison. The cyclic performance of Li|LFP full cells was tested within a voltage range of 2.5–4.3 V.

## Computational Methods

The finite element method (FEM) was used to study the distribution of Li<sup>+</sup> ions in QSHE and QSPE through COMSOL



Multiphysics 6.1. The migration of  $\text{Li}^+$  ions driven by the electric field and diffusion flow in both the quasi-solid-state polymer phase and solid phase of LATP NPs are considered [47]. FEM simulation was conducted based on the following partial differential equations for the two simplified models of electrostatic and transport of dilute species:

$$\mathbf{E} = -\nabla\varphi \quad (7)$$

$$\mathbf{N} = -D\nabla c + \mu c \mathbf{E} \quad (8)$$

$$\frac{\partial c}{\partial t} = -\nabla \mathbf{N} \quad (9)$$

where  $\mathbf{E}$  and  $\varphi$ , respectively, stand for the electric field and electric potential.  $\mathbf{N}$  is the flux vector of  $\text{Li}^+$ , and  $D$  and  $c$  are the diffusion coefficient and concentration of  $\text{Li}^+$ ,  $\mu$  is the ion mobility. The diffusion coefficients ( $D$ ) in these simplified models were calculated based on the Nernst–Einstein Equation:

$$\sigma = \frac{nz^2e^2}{k_B T} D \quad (10)$$

where  $\sigma$  is the ionic conductivity,  $n$  and  $z$  are the number of ions per unit volume and ionic valences,  $e$  is the charge of the electron,  $k_B$  and  $T$  represent the Boltzmann constant and absolute temperature. The QSPE was simplified as a sieve plate with a thickness of 30  $\mu\text{m}$ . As for the QSHE, it was simplified as a double-layer sieve plate. The upper layer is the same as QSPE, while the under layer with a thickness of 5  $\mu\text{m}$  is composed of tightly packed spherical LATP particles with a diameter of 0.3  $\mu\text{m}$  and a gap of 0.7  $\mu\text{m}$ , see illustration in Fig. S1. The current density was set to 0.02  $\text{mA cm}^{-2}$  with an applied potential difference ( $\nabla\varphi$ ) of 0.02 V. The initial  $\text{Li}^+$  ion concentration was set as 1  $\text{mol L}^{-1}$ .

## Results and Discussion

### Morphology and Structure of QSPE and QSHE

Figure 2a illustrates the synthesis process of QSHE. The LATP NPs gradually settle down to form an LATP-dominated layer during polymerization. As shown in Fig. 2b and Fig. S2, the thickness of the electrospun PVDF-HFP membrane can be tuned from ~30 to 140  $\mu\text{m}$ , which further governs the thickness of QSHE. The obtained electrospun PVDF-HFP membrane exhibits good flexibility, which can be folded multiple times without damage. SEM images (Fig. 2c, d) confirm that the randomly distributed nanofibers are successfully assembled into a 3D network with high porosity (~82.3%) (Table S1), a value

higher than ~47.7% for the commercial Celgard 2500 (Table S3). Such a membrane enables a high electrolyte uptake of ~206.5% (Table S2), which is far superior to the 86.2% of commercial separators (Table S4). The crystallinity of the prepared electrolytes was determined by XRD (Fig. S3). A wide diffraction peak between 10° and 30° of the two electrolytes represents a typical amorphous phase of polymers. Besides, the sharp XRD peaks observed in the QSHE suggest the existence of LATP NPs in the QSHE. As shown in Fig. 2e–g, the PDOL throughout fills the pores of the PVDF-HFP membrane, and an LATP-rich bottom layer can be observed, as verified by the EDS result. TGA and DSC were conducted to compare the thermal properties of QSPE and QSHE. As shown in Fig. S4, the addition of LATP has a marginal effect on the thermal stability of both electrolytes, and the  $T_g$  values are –61.03 and –61.66 °C for QSPE and QSHE, respectively, indicating that the  $\text{Li}^+$  transport is favorable in QSHE at room temperature [48]. To evaluate the mechanical properties of the synthesized electrolyte, Young's modulus of the QSPE and the top and bottom surfaces of the QSHE were measured, as displayed in Figs. S5, 2h, i. The values of each Young's modulus in the images were calculated by fitting the force curves (Fig. S6) and the histograms are displayed in Fig. S7. The average Young's modulus of the polymer-dominated surface (190.8 MPa) of QSHE is similar to that of QSPE (128.1 MPa), while the high Young's modulus of the LATP-dominated layer reached ~3.2 GPa, confirming that the inclusion of LATP NPs significantly enhances the mechanical strength of the polymer matrices, thus helping to inhibit Li dendrite growth.

Figure 3a and Fig. S8 show the polymerization of DOL initiated by  $\text{LiPF}_6$ . It can be found that the solutions change from liquid to gel after 12 h. The detailed mechanism of polymerization is presented in Fig. 3b. NMR results confirm that the chemical shifts of QSPE and QSHE are consistent with those of PDOL, suggesting the successful polymerization of DOL in QSPE and QSHE (Fig. 3c, d) [36]. As shown in the  $^1\text{H}$  spectra, the chemical shifts of the  $-\text{CH}_2-\text{CH}_2-\text{O}-$  (3.74 ppm) and  $-\text{CH}_2-\text{O}-\text{CH}_2-$  (4.75 ppm) species in DOL shifted to 3.55 and 4.59 ppm after polymerization, respectively. Meanwhile, the emergence of new e (66.99 ppm) and f (95.37 ppm) peaks in  $^{13}\text{C}$  spectra also validates the open ring polymerization of DOL. FT-IR and GPC were further carried out to support the polymerization of DOL. The characteristic peaks of DOL (918 and 1030  $\text{cm}^{-1}$ ) disappeared in QSPE/QSHE accompanied by the emergence of long-chain species (845  $\text{cm}^{-1}$ ) (Fig. 3e) [49]. Based on the GPC results, the average molecular weight and polydispersity index of QSHE were 181,344 and 1.37, respectively, which was similar to 188,967 and 1.36 of QSPE, suggesting the addition of LATP NPs does not affect the polymerization of DOL (Fig. 3f).

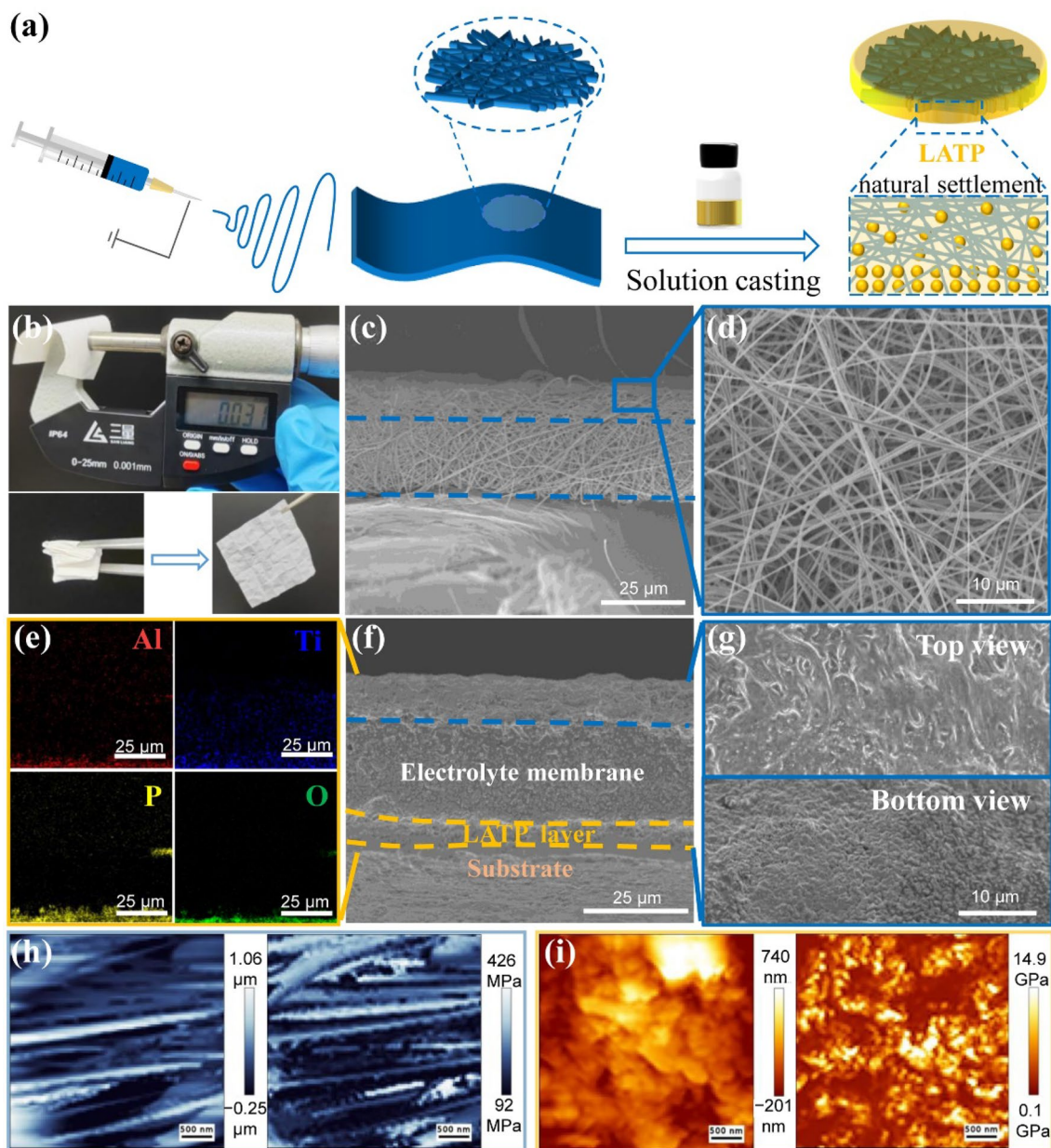


**Fig. 2** **a** Schematic showing the preparation of QSHE. **b** Digital images of the electrospun PVDF-HFP membrane and SEM images of PVDF-HFP membrane: **c** cross-section view, and **d** top view. **e** Cross-sectional element distribution in QSHE. SEM images of QSHE: **f**

cross-section, and **g** top and bottom view. **h, i** AFM images (left) and corresponding Young's modulus (right) of the top and bottom surface of QSHE

### Electrochemical Performance of QSPE and QSHE

To evaluate the properties of designed electrolytes, a couple of important metrics including ionic conductivity,  $E_a$ ,  $\text{Li}^+$  transference number, and ESW were measured. The bulk resistances of QSPE and QSHE were tested to calculate the ionic conductivity, as shown in Fig. S9. At 30 °C, QSHE exhibits an excellent ionic conductivity of  $0.98 \text{ mS cm}^{-1}$ , which is higher than that of QSPE ( $0.77 \text{ mS cm}^{-1}$ ).

Figure S9c shows the ionic conductivities of QSPE and QSHE within a wide temperature range, which are further fitted using the Vogel–Tamman–Fulcher equation. The calculated  $E_a$  for the QSHE is 0.12 eV, which is slightly lower than that for the QSPE (0.14 eV), consistent with the higher ionic conductivity of QSHE. The calculated  $t_{\text{Li}^+}$  for the QSHE is approximately 0.62, which is slightly higher than that of QSPE (Fig. 3g, h). The high  $t_{\text{Li}^+}$  in QSHE can be ascribed to the entrapment of large TFSI<sup>-</sup> anions by the

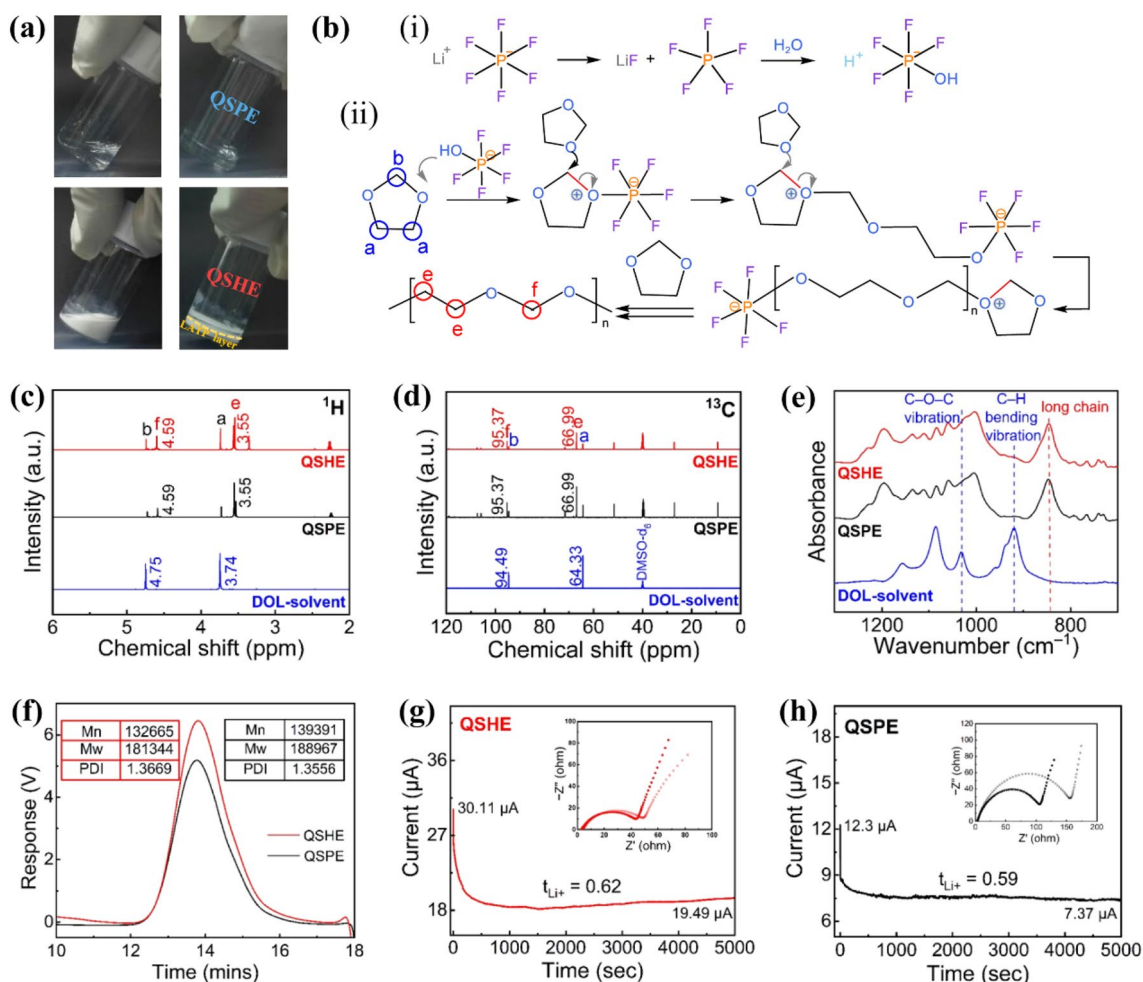


**Fig. 3** **a** Digital images of QSPE and QSHE. **b** (i) The hydrolysis process of  $\text{LiPF}_6$  and (ii) the polymerization mechanism of DOL. **c**  $^1\text{H}$ -NMR, **d**  $^{13}\text{C}$ -NMR spectra, and **e** FTIR spectroscopy of DOL, QSPE,

and QSHE. **f** GPC profiles of QSPE and QSHE. Chronoamperometric and Nyquist plots (inset) of **g** QSHE and **h** QSPE

PVDF-HFP [50] and PDOL network [48], as well as the fast  $\text{Li}^+$  transport in LAMP. Except for high  $\text{Li}^+$  conductivity, the electrochemical stability of the electrolyte is also critical for stable battery cycling. The LSV results in Fig. S10 demonstrate the ESWs of QSPE and QSHE are 4.60 and 4.76 V, respectively. The wide ESW can be attributed to the polymerized long chains and the addition of LAMP fillers [51].

Furthermore,  $\text{Li|QSHE|Cu}$  and  $\text{Li|QSPE|Cu}$  cells were assembled to assess the Li plating/stripping efficiencies. Figure 4a–c shows that the QSHE exhibited a stable CE of  $\approx 94\%$  over 140 cycles at  $0.5 \text{ mA cm}^{-2}$  with a smaller overpotential, while the CE of QSPE dropped significantly to below 84%. The compatibility between the Li anode and the designed electrolytes was further investigated. Compared to the  $\text{Li|QSPE|Li}$  symmetric cell, the bulk and interface resistances of the  $\text{Li|QSHE|Li}$  cell increased slightly after a 100-h cycle (Fig. 4d, e). The critical current density (CCD) was determined by increasing the plating/stripping current

densities from  $0.05$  to  $2 \text{ mA cm}^{-2}$  with a fixed capacity of  $1 \text{ mAh cm}^{-2}$  in  $\text{Li|QSHE|Li}$  and  $\text{Li|QSPE|Li}$  symmetric cells. Figure 4f shows that the QSHE operated stably until the current density reached  $1.3 \text{ mA cm}^{-2}$ , which was significantly higher than that in QSPE ( $0.4 \text{ mA cm}^{-2}$ ). Besides, the  $\text{Li|QSHE|Li}$  symmetric cells displayed stable polarization voltages of  $\sim 20$  and  $40 \text{ mV}$  without a significant increase for more than 2000 h at  $0.1$  and  $0.2 \text{ mA cm}^{-2}$ , respectively (Fig. 4g and S11). In contrast, short circuits occurred quickly in  $\text{Li|QSPE|Li}$  cells, manifesting the inferior interface stability of QSPE against Li metal anode compared to QSHE.

### Electrochemical Performance of $\text{Li|LFP}$ Full Cells

CV tests of  $\text{Li|LFP}$  batteries employing QSPE and QSHE at different scan rates were conducted at a scan rate of  $0.1 \text{ mV s}^{-1}$ . Figure 5a shows the use of QSHE electrolyte in  $\text{Li|LFP}$  batteries results in an oxidation/reduction



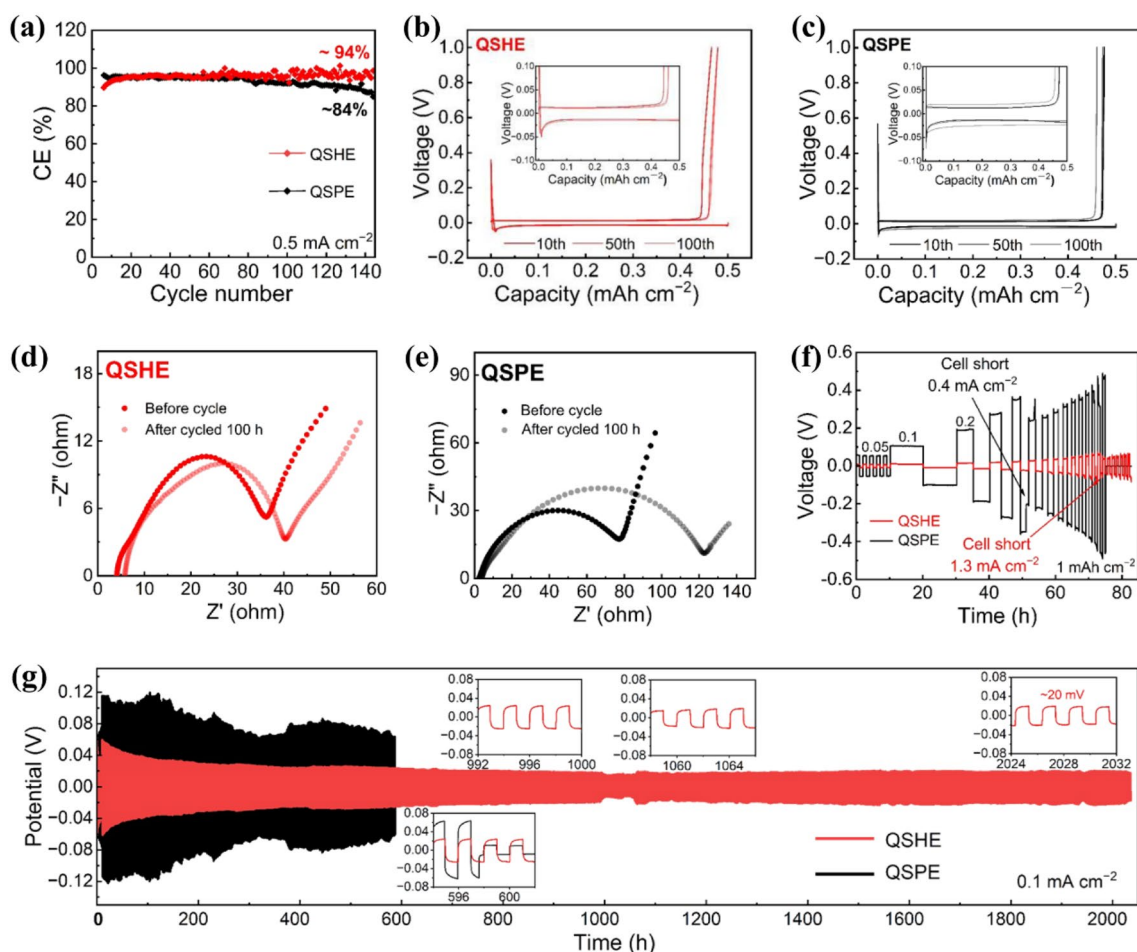


**Fig. 4** a CEs of LiQSHE/Cu and LiQSPE/Cu cells. Li plating/stripping curves of **b** LiQSHE/Cu and **c** LiQSPE/Cu cells. Nyquist plots of **d** LiQSHE/Li and **e** LiQSPE/Li cells before and after cycles.

Polarization curves of symmetric LiQSHE/Li and LiQSPE/Li cells, **f** rate performance, and **g** long-term stability at  $0.1 \text{ mA cm}^{-2}$  for  $0.1 \text{ mAh cm}^{-2}$  of LiQSHE/Li cells

voltage gap of  $\sim 0.24 \text{ V}$ , outperforming the QSPE counterpart ( $\sim 0.32 \text{ V}$ ). As the scan rate increased, the polarization of Li/LFP batteries increased (Fig. S12). The QSHE and QSPE exhibited  $D_{\text{Li}^+}$  values in the order of  $10^{-9} \text{ cm}^2 \text{ s}^{-1}$ , as calculated based on Eq. (5) (Fig. 5b), surpassing  $10^{-13} \text{ cm}^2 \text{ s}^{-1}$  of commercial electrolytes [34]. The Nyquist plots of LiQSHE/LFP and LiQSPE/LFP cells in Fig. 5c showed that QSHE has a smaller initial interface impedance and is more stable against Li compared to QSPE, which could be attributed to the fast  $\text{Li}^+$  transport at the interface supported by LATP NPs. The detailed values of fitted bulk and interphase resistances are reported in Table S5. Besides, the Li/LFP batteries using QSPE and QSHE were also assembled to evaluate the cyclic and rate performance. The QSHE enabled the battery to deliver an initial discharge capacity of  $144.9 \text{ mAh g}^{-1}$  at  $0.5 \text{ C}$ , which slightly increased to  $148.5 \text{ mAh g}^{-1}$  (Fig. S13a). A similar trend was also observed for the Li/LFP battery using QSPE, whose discharge capacity increased from

$140.9$  to  $144.9 \text{ mAh g}^{-1}$  during the initial activation process. When the current density was increased to  $2 \text{ C}$ , the battery using QSHE presented an initial discharge capacity of  $128.6 \text{ mAh g}^{-1}$ , accompanied by a high capacity retention of  $95.4\%$  after  $300$  cycles (Fig. 5d). By contrast, the QSPE-based Li/LFP battery delivered a discharge capacity of  $118.6 \text{ mAh g}^{-1}$  and maintained  $77.7\%$  of initial capacity after  $300$  cycles. The charge–discharge curves in Fig. S13b and S13c also manifested that the LiQSHE/LFP battery possessed smaller polarization voltages and more stable cyclic performance than the LiQSPE/LFP counterpart. Moreover, the Li/LE/LFP battery exhibited fast capacity decay, which can be attributed to the formation of unstable SEI and the corrosion of Li in commercial LE (Fig. S14a). After  $300$  cycles, the cell exhibited a reversible capacity of  $121.1 \text{ mAh g}^{-1}$ , corresponding to a capacity retention rate of  $77.6\%$  (Fig. S14b). Therefore, the design of a LATP-rich layer towards Li metal in heterogeneous QSHE can promote uniform Li deposition/dissolution and prevent Li



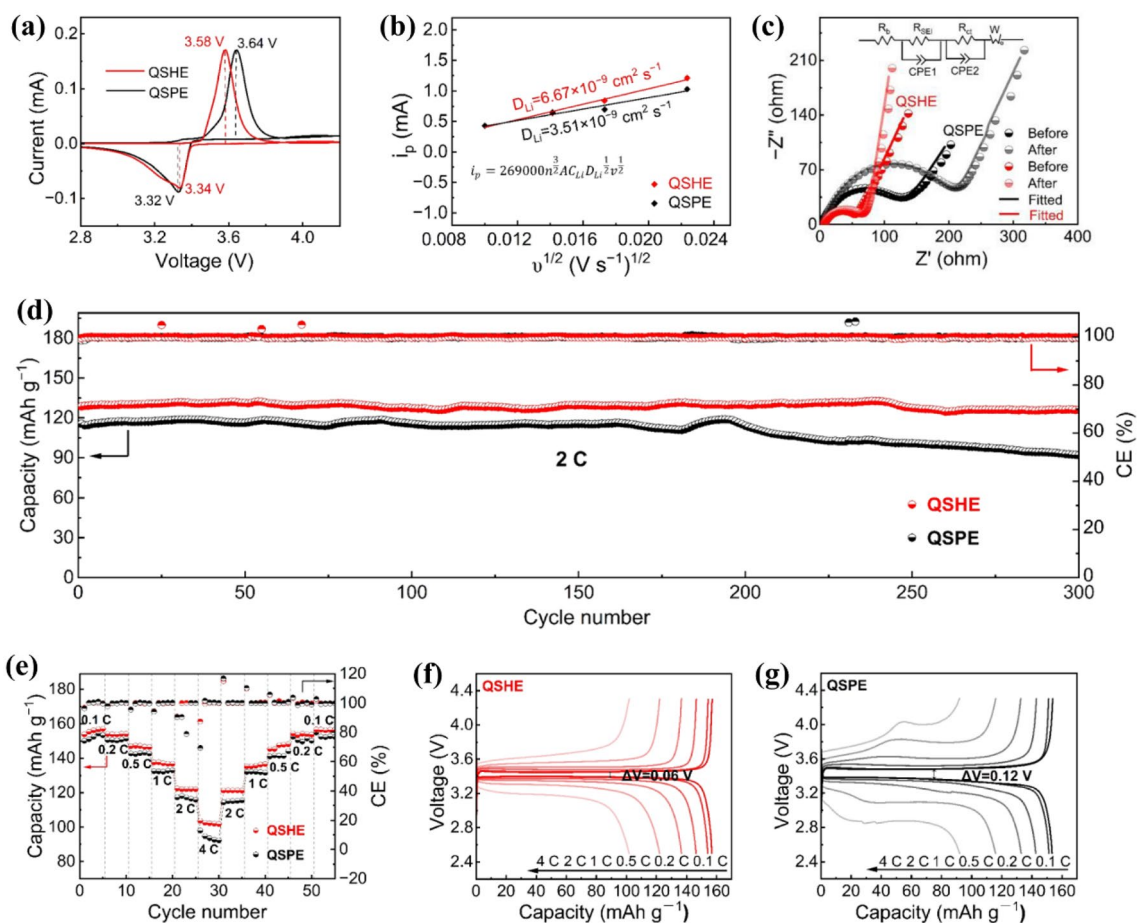


**Fig. 5** Electrochemical performance of Li|QSHE|LFP and Li|QSPE|LFP cells. **a** CV curves at  $0.1 \text{ mV s}^{-1}$ . **b** The fitting curves between CV peak current data as a function of the square root of scan

rate. **c** Nyquist plots before and after cycles. **d** Cyclic performance at 2 C. **e** Rate capability and corresponding charge–discharge curves of Li|LFP batteries using **f** QSHE and **g** QSPE

dendrite growth during the charging/discharging process, hence extending the lifespan of Li metal batteries. The pressure applied for cell assembly was also investigated since the pressure has a significant impact on the mechanical and electrochemical performance of solid-state batteries. As shown in Fig. S15, with an assembly pressure ranging from 400–750 MPa, the Li|QSHE|LFP delivered comparable capacities at 2 C. The Li|LFP batteries exhibited much the same reversible capacities at low current densities (0.1, 0.2, 0.5 C) whenever QSPE or QSHE was used (Fig. 5e). Notably, at a high current density of 4 C, the Li|LFP battery with QSPE displayed a capacity of only  $\sim 95 \text{ mAh g}^{-1}$ , while the cell using QSHE retained a capacity of  $\sim 102 \text{ mAh g}^{-1}$ . The corresponding charge–discharge profiles in Fig. 5f and g confirm the cell with QSHE exhibited smaller voltage hysteresis. At current densities of 2 and 4 C, the cells with QSHE displayed polarization voltages of 0.25 and 0.51 V, respectively, which are much smaller than 0.7 and 1.16 when QSPE was applied.

## Lithium Metal Morphology and SEI Chemistries

To clarify the ion transport manipulated by the LATP layer in QSHE, COMSOL Multiphysics was applied to monitor the  $\text{Li}^+$  ion distribution after charging. As shown in Fig. 6a, a large concentration gradient difference was formed during the charging process in QSPE, which increases the transport barrier and polarization of  $\text{Li}^+$ . On the contrary, the inclusion of LATP NPs mitigates the  $\text{Li}^+$  concentration gradient in QSHE (Fig. 6b), offering fast and abundant  $\text{Li}^+$  transport channels [47]. To this end, smooth and dense Li deposition was achieved during repeated charge–discharge processes.

SEM and XPS were carried out to further study the morphology evolution of cycled Li metal anodes and SEI chemistry on Li anodes. Large cracks and mossy Li were observed on the surface after only 10 cycles when the commercial LE was used, indicating its poor compatibility with metallic Li (Fig. S16). When QSPE was used, many “dead” Li can be observed, indicating the PDOL with a low Young’s

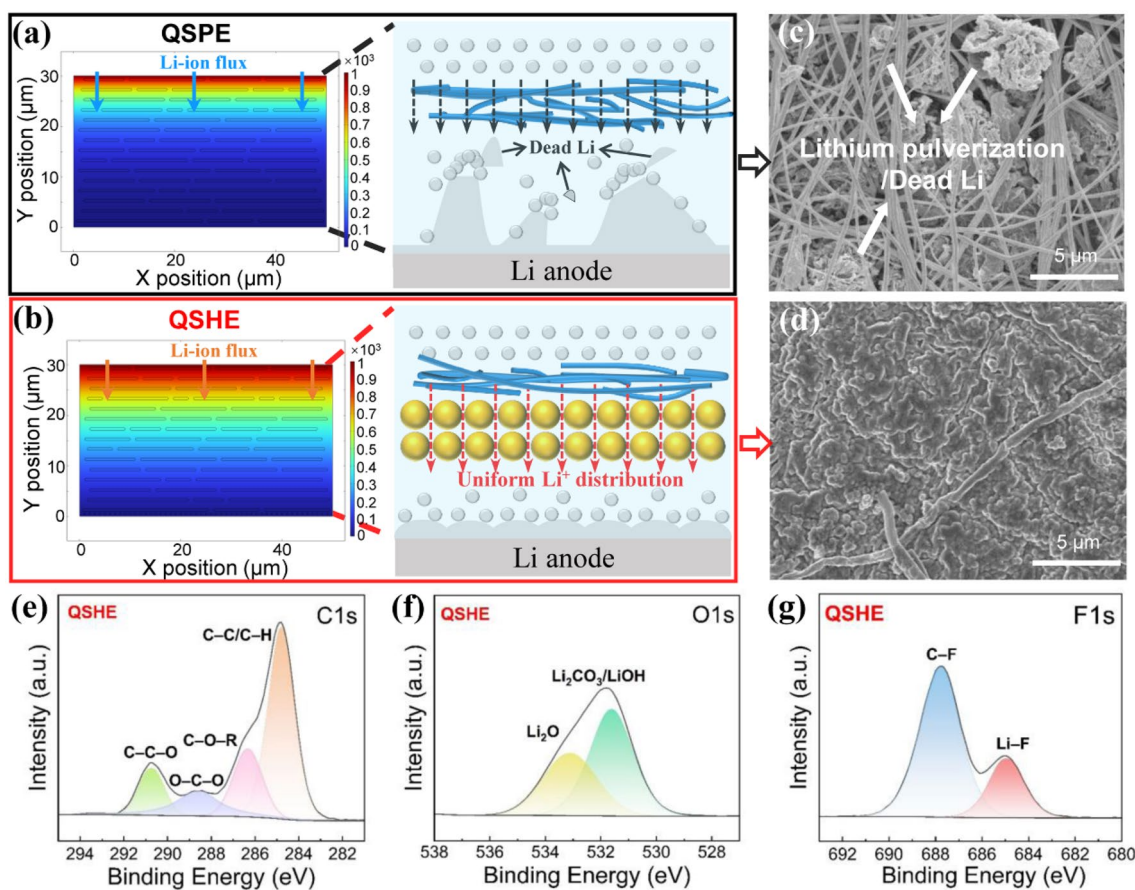


**Fig. 6** Simulation results and schematic diagram of Li<sup>+</sup> ion distribution in **a** QSPE and **b** QSHE; SEM images of the Li metal surface of **c** QSPE and **d** QSHE after cycling; XPS of cycled Li metal in QSHE: **e** C 1s, **f** O 1s, **g** F 1s

modulus cannot effectively prevent the growth of Li dendrites (Fig. 6c). In contrast, the heterogeneous QSHE with a LAMP-rich bottom layer enabled reversible deposition of Li on pristine Li metal anode, verifying the importance of introducing a robust inorganic layer to promote the uniform distribution and fast transport of Li<sup>+</sup> (Fig. 6d). Meanwhile, the EDS mapping proved that LAMP NPs are absent on the Li metal surface (Fig. S17). Furthermore, the SEI chemistry on Li metal was elucidated through XPS (Fig. 6e–g and Fig. S18). In the C 1s spectra, the typical peak at 284.8 eV represents the C–C/C–H bond, while the peaks at 286.3, 288.5, and 290.7 eV correspond to C–O–R, O–C–O, and C–C–O bonds, respectively, which were derived from the –CH<sub>2</sub>CH<sub>2</sub>OCH<sub>2</sub>O– unit of PDOL [32, 52]. Besides, the additional peak of Li<sub>2</sub>CO<sub>3</sub> suggested a relatively unstable SEI layer of QSPE. The O 1s spectra can be deconvoluted into two peaks at 531 and 532.6 eV, corresponding to Li<sub>2</sub>O and Li<sub>2</sub>CO<sub>3</sub>/LiOH [53, 54]. Moreover, the higher content of Li<sub>2</sub>O in QSHE may originate from the slight reaction of Li metal with LAMP NPs during the polymerization process [43], which not only enhances the stability of SEI but also facilitates Li<sup>+</sup> transport [33], differing from the large amount

of unstable LiOH in QSPE. Meanwhile, the peaks near 684.9 and 687.8 eV in the F 1s spectra are related to Li–F and C–F bonds [53], which can be attributed to the decomposition of FEC, LiTFSI, and LiPF<sub>6</sub>. Therefore, the introduction of LAMP alleviates the decomposition of Li salts and FEC, which leads to the formation of a proper amount of lithium fluoride (LiF) in the SEI [33, 55]. As a result, the SEI layer containing inorganic and organic components combined with the LAMP layer in QSHE can effectively adapt to the volume change during cycles and inhibit the growth of Li dendrites for long-term cycles.

## Conclusions

In conclusion, a heterogeneous QSHE with a LAMP-rich bottom layer was prepared through in situ polymerization of DOL using electrospun PVDF-HFP as the skeleton. In such an electrolyte, the incorporation of LAMP NPs not only improves the overall ionic conductivity (0.98 mS cm<sup>−1</sup> at 30 °C) but also enhances Young's modulus of the QSHE's bottom layer facing Li metal. In addition, FEM results

confirm that the LATP NPs promote a more uniform distribution of  $\text{Li}^+$  throughout the electrolyte, contributing to uniform Li deposition. Consequently, the Li|QSHE|Li cells displayed ultra-long cycle stability over 2000 h at both 0.1 and 0.2 mA  $\text{cm}^{-2}$ . Furthermore, the Li|QSHE|LFP cell demonstrated excellent cyclic stability with a capacity retention rate of 95.4% after 300 cycles at 2 C. The design concept of heterogeneous QSSEs provides an appealing pathway towards high-energy-density and long-life Li metal batteries.

**Supplementary Information** The online version contains supplementary material available at <https://doi.org/10.1007/s42765-023-00371-8>.

**Acknowledgements** This project was supported by the National Natural Science Foundation of China (No. 22179022, No. 22109023, and No.22209027), the Industry-University Research Joint Innovation Project of Fujian Province (No. 2021H6006), the FuXiaQuan National Independent Innovation Demonstration Zone Collaborative Innovation Platform (No. 2022-P-027), the Youth Innovation Fund of Fujian Province (No. 2021J05043 and No.2022J05046), the Award Program for Fujian Minjiang Scholar Professorship.

**Data Availability** All data are available upon reasonable request.

## Declarations

**Conflict of Interest** YMC is an editorial board member for Advanced Fiber Materials and was not involved in the editorial review or the decision to publish this article. All authors declare that there are no competing interests.

## References

- Chen Y, Xu M, Huang Y, Manthiram A. Creating a rechargeable world. *Chemistry*. **2022**;8:312.
- Ma L, Chen H, Wu J, Lv Y, Chen X, Li X, Li QJ, Di J, Chen Y. Recent progress on zeolitic imidazolate frameworks and their derivatives in alkali metal-chalcogen batteries. *Adv Energy Mater*. **2021**;12:2103152.
- Li C, Tong L, Wang S, Liu Q, Wang Y, Li X, Wang M, Li M, Chen X, Wu J, Chen Q, Mai YW, Fan W, Chen Y, Li X. Nitrogen doping induced by intrinsic defects of recycled polyethylene terephthalate-derived carbon nanotubes. *SusMat*. **2023**;3:431.
- Iqbal H, Sarwar S, Kirli D, Shek JKH, Kiprakis AE. A survey of second-life batteries based on techno-economic perspective and applications-based analysis. *Carbon Neutrality*. **2023**;2:8.
- Ma L, Lv Y, Wu J, Chen Y, Jin Z. recent advances in emerging non-lithium metal-sulfur batteries: a review. *Adv Energy Mater*. **2021**;11:2100770.
- Wang Z, Li X, Chen Y, Pei K, Mai Y-W, Zhang S, Li J. Creep-enabled 3D solid-state lithium-metal battery. *Chemistry*. **2020**;6:2878.
- Wu J, He J, Wang M, Li M, Zhao J, Li Z, Chen H, Li X, Li C, Chen X, Li X, Mai YW, Chen Y. Electrospun carbon-based nanomaterials for next-generation potassium batteries. *Chem Commun*. **2023**;59:2381.
- Li M, Chen H, Wang Y, Chen X, Wu J, Su J, Wang M, Li X, Li C, Ma L, Li X, Chen Y. Two birds with one stone: engineering siloxane-based electrolytes for high-performance lithium-sulfur polyacrylonitrile batteries. *J Mater Chem A*. **2023**;11:11721.
- Li C, Qiu M, Li R, Li X, Wang M, He J, Lin G, Xiao L, Qian Q, Chen Q, Wu J, Li X, Mai Y-W, Chen Y. Electrospinning engineering enables high-performance sodium-ion batteries. *Adv Fiber Mater*. **2022**;4:43.
- Xu X, Cheng X, Jiang F, Yang S, Ren D, Shi P, Hsu H, Yuan H, Huang J, Ouyang M, Zhang Q. Dendrite-accelerated thermal runaway mechanisms of lithium metal pouch batteries. *SusMat*. **2022**;2:435.
- Chen Y, Wang Z, Li X, Yao X, Wang C, Li Y, Xue W, Yu D, Kim SY, Yang F, Kushima A, Zhang G, Huang H, Wu N, Mai YW, Goodenough JB, Li J. Li metal deposition and stripping in a solid-state battery via Coble creep. *Nature*. **2020**;578:251.
- Wang M, Wu Y, Qiu M, Li X, Li C, Li R, He J, Lin G, Qian Q, Wen Z, Li X, Wang Z, Chen Q, Chen Q, Lee J, Mai YW, Chen Y. Research progress in electrospinning engineering for all-solid-state electrolytes of lithium metal batteries. *J Energy Chem*. **2021**;61:253.
- Li X, Chen W, Qian Q, Huang H, Chen Y, Wang Z, Chen Q, Yang J, Li J, Mai YW. Electrospinning-based strategies for battery materials. *Adv Energy Mater*. **2020**;11:2000845.
- Yan C-L. Realizing high performance of solid-state lithium metal batteries by flexible ceramic/polymer hybrid solid electrolyte. *Rare Met*. **2020**;39:458.
- Yu Q, Jiang K, Yu C, Chen X, Zhang C, Yao Y, Jiang B, Long H. Recent progress of composite solid polymer electrolytes for all-solid-state lithium metal batteries. *Chin Chem Lett*. **2021**;32:2659.
- Wu J, Chen X, Fan W, Li X, Mai Y-W, Chen Y. Rationally designed alloy phases for highly reversible alkali metal batteries. *Energy Stor Mater*. **2022**;48:223.
- Zhang H, Chen Y, Li C, Armand M. Electrolyte and anode-electrolyte interphase in solid-state lithium metal polymer batteries: a perspective. *SusMat*. **2021**;1:24.
- Yan C, Zhu P, Jia H, Zhu J, Selvan RK, Li Y, Dong X, Du Z, Angunawela I, Wu N, Dirican M, Zhang X. High-performance 3D fiber network composite electrolyte enabled with Li-ion conducting nanofibers and amorphous PEO-based cross-linked polymer for ambient all-solid-state lithium-metal batteries. *Adv Fiber Mater*. **2019**;1:46.
- Liu Q, Han X, Wei G, Zhang H, Li Y, Li J, He X. Inorganic composites improving conductivities of solid polymer electrolytes for lithium batteries: a review. *ChemNanoMat*. **2023**;9: e202300202.
- Wei C, Liu X, Yu C, Chen S, Chen S, Cheng S, Xie J. Revealing performance of 78Li2S-22P2S5 glass-ceramic based solid-state batteries at different operating temperatures. *Chin Chem Lett*. **2023**;34: 107859.
- Wang G, Liang Y, Liu H, Wang C, Li D, Fan L-Z. Scalable, thin asymmetric composite solid electrolyte for high-performance all-solid-state lithium metal batteries. *Interdiscip Mater*. **2022**;1:434.
- Zhu J, He S, Tian H, Hu Y, Xin C, Xie X, Zhang L, Gao J, Hao S, Zhou W, Zhang L. The influences of DMF content in composite polymer electrolytes on Li<sup>+</sup>-conductivity and interfacial stability with Li-metal. *Adv Funct Mater*. **2023**;33:2301165.
- Wang L, Shi H, Xie Y, Wu Z-S. Fluorinated boron nitride nanosheet enhanced ultrathin and conductive polymer electrolyte for high-rate solid-state lithium metal batteries. *Interdiscip Mater*. **2023**;2:789.
- Yan W, Gao X, Jin X, Liang S, Xiong X, Liu Z, Wang Z, Chen Y, Fu L, Zhang Y, Zhu Y, Wu Y. Nonporous gel electrolytes enable long cycling at high current density for lithium-metal anodes. *ACS Appl Mater Interfaces*. **2021**;13:14258.
- Zhijie B, Xiangxin G. Solidification for solid-state lithium batteries with high energy density and long cycle life. *Energy Mater*. **2022**;2: 200011.
- Xie X, Wang Z, He S, Chen K, Huang Q, Zhang P, Hao SM, Wang J, Zhou W. Influencing factors on li-ion conductivity and interfacial stability of solid polymer electrolytes, exemplified by



- polycarbonates, polyoxalates, and polymalonates. *Angew Chem Int Ed.* **2023**;135: e202218229.
27. Matteo P, Akiko T, Henry A, Maria Assunta N, Stefano P. Ionic liquids and their derivatives for lithium batteries: role, design strategy, and perspectives. *Energy Mater.* **2023**;3: 300049.
  28. Wang S, Zhang J, Hua W, Wen L, Tang G, Wang X, Ma C, Chen W. Solvation-enhanced electrolyte on layered oxide cathode tailoring even and stable CEI for durable sodium storage. *Carbon Neutrality.* **2023**;2:20.
  29. Cheng H, Yan C, Orenstein R, Dirican M, Wei S, Subjalearndee N, Zhang X. Polyacrylonitrile nanofiber-reinforced flexible single-ion conducting polymer electrolyte for high-performance, room-temperature all-solid-state Li-metal batteries. *Adv Fiber Mater.* **2022**;4:532.
  30. Wang L, Xu S, Wang Z, Yang E, Jiang W, Zhang S, Jian X, Hu F. A nanofiber–gel composite electrolyte with high Li<sup>+</sup> transference number for application in quasi-solid batteries. *eScience.* **2023**;3: 100090.
  31. Yang Y, Yang W, Yang H, Zhou H. Electrolyte design principles for low-temperature lithium-ion batteries. *eScience.* **2023**;3: 100170.
  32. Yu J, Lin X, Liu J, Yu JTT, Robson MJ, Zhou G, Law HM, Wang H, Tang BZ, Ciucci F. In situ fabricated quasi-solid polymer electrolyte for high-energy-density lithium metal battery capable of subzero operation. *Adv Energy Mater.* **2021**;12:2102932.
  33. Chen D, Zhu M, Kang P, Zhu T, Yuan H, Lan J, Yang X, Sui G. Self-enhancing gel polymer electrolyte by in situ construction for enabling safe lithium metal battery. *Adv Sci.* **2022**;9: e2103663.
  34. Liu F, Li T, Yang Y, Yan J, Li N, Xue J, Huo H, Zhou J, Li L. Investigation on the copolymer electrolyte of poly(1,3-dioxolane-co-formaldehyde). *Macromol Rapid Commun.* **2020**;41:2000047.
  35. Liu Q, Cai B, Li S, Yu Q, Lv F, Kang F, Wang Q, Li B. Long-cycling and safe lithium metal batteries enabled by the synergistic strategy of ex-situ anodic pretreatment and an in-built gel polymer electrolyte. *J Mater Chem A.* **2020**;8:7197.
  36. Liu F, Wang W, Yin Y, Zhang S, Shi J, Wang L, Zhang X, Zheng Y, Zhou J, Li L, Guo Y. Upgrading traditional liquid electrolyte via in situ gelation for future lithium metal batteries. *Sci Adv.* **2018**;4:eaat5383.
  37. Li L, Li R, Huang Z, Liu M, Xiang J, Shen X, Jing M. High-performance gel electrolyte for enhanced interface compatibility and lithium metal stability in high-voltage lithium battery. *Colloid Surface A.* **2022**;651: 129665.
  38. Ma Q, Yue J, Fan M, Tan S, Zhang J, Wang W, Liu Y, Tian Y, Xu Q, Yin Y, You Y, Luo A, Xin S, Wu X, Guo Y. Formulating the electrolyte towards high-energy and safe rechargeable lithium-metal batteries. *Angew Chem Int Ed.* **2021**;60:16554.
  39. Huang K, Bi S, Xu H, Wu L, Fang C, Zhang X. Optimizing Li-ion solvation in gel polymer electrolytes to stabilize Li-metal anode. *Chemsuschem.* **2023**;16(19): e202300671.
  40. Rath PC, Liu M, Lo S, Dhaka RS, Bresser D, Yang C, Lee S, Chang JK. Suppression of dehydrofluorination reactions of a Li<sub>0.33</sub>La<sub>0.557</sub>TiO<sub>3</sub>-nanofiber-dispersed poly(vinylidene fluoride-co-hexafluoropropylene) electrolyte for quasi-solid-state lithium-metal batteries by a fluorine-rich succinonitrile interlayer. *ACS Appl Mater Interfaces.* **2023**;15:15429.
  41. Chen H, Li M, Li C, Li X, Wu Y, Chen X, Wu J, Li X, Chen Y. Electrospun carbon nanofibers for lithium metal anodes: progress and perspectives. *Chin Chem Lett.* **2022**;33:141.
  42. Li X, Chen Y, Huang H, Mai YW, Zhou L. Electrospun carbon-based nanostructured electrodes for advanced energy storage—a review. *Energy Storage Mater.* **2016**;5:58.
  43. Chen Z, Kim GT, Kim JK, Zarrabeitia M, Kuenzel M, Liang H, Geiger D, Kaiser U, Passerini S. Highly stable quasi-solid-state lithium metal batteries: reinforced Li<sub>1.3</sub>Al<sub>0.3</sub>Ti<sub>1.7</sub>(PO<sub>4</sub>)<sub>3</sub>/Li interface by a protection interlayer. *Adv Energy Mater.* **2021**;11:2101339.
  44. Chen L-H, Huang Z-Y, Chen S-L, Tong R-A, Wang H-L, Shao G, Wang C-A. In situ polymerization of 1,3-dioxolane infiltrating 3D garnet framework with high ionic conductivity and excellent interfacial stability for integrated solid-state Li metal battery. *Rare Met.* **2022**;41:3694.
  45. Xia M, Liu Q, Zhou Z, Tao Y, Li M, Liu K, Wu Z, Wang D. A novel hierarchically structured and highly hydrophilic poly(vinyl alcohol-co-ethylene)/poly(ethylene terephthalate) nanoporous membrane for lithium-ion battery separator. *J Power Sources.* **2014**;266:29.
  46. Li S, Chen Y-M, Liang W, Shao Y, Liu K, Nikolov Z, Zhu Y. A superionic conductive electrochemically stable dual-salt polymer electrolyte. *Joule.* **2018**;2:2018:2.
  47. Zhao C, Chen P, Zhang R, Chen X, Li B-Q, Zhang X, Cheng X, Zhang Q. An ion redistributor for dendrite-free lithium metal anodes. *Sci Adv.* **2018**;4:eaat3446.
  48. Cui J, Du Y, Zhao L, Li X, Sun Z, Li D, Li H. Thermal stable poly-dioxolane based electrolytes via a robust crosslinked network for dendrite-free solid-state Li-metal batteries. *Chem Eng J.* **2023**;461: 141973.
  49. Zhao Q, Liu X, Stalin S, Khan K, Archer LA. Solid-state polymer electrolytes with in-built fast interfacial transport for secondary lithium batteries. *Nat Energy.* **2019**;4:365.
  50. Liu W, Yi C, Li L, Liu S, Gui Q, Ba D, Li Y, Peng D, Liu J. Designing polymer-in-salt electrolyte and fully infiltrated 3D electrode for integrated solid-state lithium batteries. *Angew Chem Int Ed.* **2021**;60:12931.
  51. Rajendran S, Tang Z, George A, Cannon A, Neumann C, Sawas A, Ryan E, Turchanin A, Arava LMR. Inhibition of lithium dendrite formation in lithium metal batteries via regulated cation transport through ultrathin sub-nanometer porous carbon nanomembranes. *Adv Energy Mater.* **2021**;11:2100666.
  52. Wang Y, Lin C, Rao J, Gaskell K, Rubloff G, Lee SB. Electrochemically controlled solid electrolyte interphase layers enable superior Li–S batteries. *ACS Appl Mater Interfaces.* **2018**;10:24554.
  53. Didwal PN, Singhbabu YN, Verma R, Sung B-J, Lee G-H, Lee J-S, Chang DR, Park C-J. An advanced solid polymer electrolyte composed of poly(propylene carbonate) and mesoporous silica nanoparticles for use in all-solid-state lithium-ion batteries. *Energy Storage Mater.* **2021**;37:476.
  54. Wang H, Wang Q, Cao X, He Y, Wu K, Yang J, Zhou H, Liu W, Sun X. Thiol-branched solid polymer electrolyte featuring high strength, toughness, and lithium ionic conductivity for lithium-metal batteries. *Adv Mater.* **2020**;32:2001259.
  55. Gao Y, Yan Z, Gray JL, He X, Wang D, Chen T, Huang Q, Li YC, Wang H, Kim SH, Mallouk TE, Wang D. Polymer–inorganic solid–electrolyte interphase for stable lithium metal batteries under lean electrolyte conditions. *Nat Mater.* **2019**;18:384.

**Publisher's Note** Springer Nature remains neutral with regard to jurisdictional claims in published maps and institutional affiliations.

Springer Nature or its licensor (e.g. a society or other partner) holds exclusive rights to this article under a publishing agreement with the author(s) or other rightsholder(s); author self-archiving of the accepted manuscript version of this article is solely governed by the terms of such publishing agreement and applicable law.